A numerical study on the influence of crossflow transition on a marine propeller in open water

Ocean Engineering 310 (2024) 118573

Contents lists available at ScienceDirect

Ocean Engineering

journal homepage: www.elsevier.com/locate/oceaneng

Research paper

A numerical study on the influence of crossflow transition on a marine propeller in open water

Rui Lopes [a,*], Arash Eslamdoost [a], Rikard Johansson [b], Seemontini RoyChoudhury [b], Rickard E. Bensow [a]

[a] Chalmers University of Technology, Department of Mechanics and Maritime Sciences, Gothenburg, Sweden
[b] Kongsberg Maritime Hydrodynamic Research Centre, Kongsberg Maritime Sweden AB, Kristinehamn, Sweden

ARTICLE INFO

Keywords:
RANS
Crossflow transition
Turbulence
Model-scale propeller

ABSTRACT

This work studies the influence of crossflow transition modelling on the performance and flow field of a controllable pitch propeller. The simulations are performed for two different crossflow terms, and baseline simulations without crossflow transition are performed as well. The results show that in the absence of a crossflow term, the flow over the propeller blades is almost fully laminar. When a crossflow term is included, a significant part of the flow becomes turbulent, thus causing a decrease in the thrust and torque coefficients. The change in the propeller performance is also due to the absence of laminar flow separation near the trailing edge, which is prevented when transition occurs upstream of that location due to crossflow. The comparison between the two crossflow terms shows that one always leads to a larger extent of turbulent flow and earlier transition than the other, although this not always translates in lower thrust and torque, depending on the considered advance coefficient. This illustrates the delicate balance in the effects taking place on the pressure and suction side of the propeller blades, and the importance of correctly including crossflow effects in simulations of model-scale propellers.

1. Introduction

The design of a marine propeller is often supported at a final stage by model scale testing, as a way to assess the performance of the propeller. Naturally, due to physical limitations, the model scale tests are conducted at a Reynolds number much lower than that experienced by the full scale geometry. The Reynolds number of the model scale tests, around 10^5, implies that a large part of the boundary layer developing on the surface of the propeller blades is in the laminar regime (Baltazar et al., 2018), unlike what is observed at full scale. This is sometimes avoided at model scale through the use of a tripping method such as roughness or trip wires at the leading edge to trigger transition, so that the flow can be considered as fully turbulent.

With the computational power and tools currently available, Computational Fluid Dynamics (CFD) is becoming a practical tool to assess propeller performance, both at model scale and at full scale. Although it is much easier to conduct a full scale CFD simulation than a full scale experimental measurement, confidence must be established in the CFD approach and corresponding models and assumptions, such as turbulence models. This is usually done through the comparison of results of model scale simulations with their experimental counterparts. Hence, even for CFD, model scale runs are still indispensable and very valuable.

The difficulties associated with laminar flow at model scale are also present in CFD simulations. When these are compared with experiments where the flow was tripped, the use of a well-established turbulence model tends to lead to acceptable results. Even for moderate Reynolds numbers of the order of 10^5, traditionally used turbulence models such as $k-\omega$ models lead to negligible extents of laminar flow (Wilcox, 2004), which are confined to a small region near the leading edge of the blade. However, if the flow is not tripped, then this approach is no longer adequate, and poor agreement is obtained between the fully turbulent solution obtained in the CFD simulation and the transitional flow that is observed in the experiments. The inability of turbulence models to lead to accurate results in these circumstances is not surprising, as they are developed for use at high Reynolds number flows. Their calibration relies on classical results such as the log law and fully turbulent channel flow, which are not valid for laminar flow, and the models make no attempt at predicting the onset of transition.

The accurate prediction of laminar to turbulent transition has been a challenge for CFD for a long time. The method that has seen the most

* Corresponding author.
E-mail address: rui.lopes@chalmers.se (R. Lopes).

https://doi.org/10.1016/j.oceaneng.2024.118573
Received 2 February 2024; Received in revised form 28 May 2024; Accepted 23 June 2024
Available online 3 July 2024

success has been the e^N method, developed independently by Smith & Gamberoni and Van Ingen (Smith and Gamberoni, 1956; van Ingen, 1956). The e^N method is based on linear stability theory, and consists of tracking the growth of a disturbance in the flow along the streamlines, ultimately leading to transition when a certain growth amplitude is achieved. Despite its theory-based formulation, it still requires some calibration in the form of the critical growth that is considered to start transition. The e^N method is typically used with boundary-layer codes, which provide highly resolved velocity profiles as required by the method. Furthermore, it uses several non-local operations which are generally incompatible with modern CFD codes that heavily rely on parallel processing and domain decomposition.

This last point illustrates one of the main reasons for the difficulty in the modelling of transition with CFD. Many of the available empirical correlations for transition depend on quantities like the momentum thickness Reynolds number (Abu-Ghannam and Shaw, 1980), which require integration in the boundary layer. This translates into some of the first models developed for transition (Suzen and Huang, 2000). Other alternatives, such as low Reynolds number variants of turbulence models (Jones and Launder, 1973) have been shown to work solely due to the resemblance between the viscous sublayer in turbulent flow and the laminar boundary layer, which hardly makes them suitable for transition prediction (Rumsey et al., 2006).

In spite of the previously mentioned difficulties, the area of transition modelling has undergone a significant advancement with the development and publication of models that rely only on local variables. One of these models is the $\gamma - Re_\theta$ model (Langtry and Menter, 2009), based on correlations but with a fully local formulation and capable of accounting for transition mechanisms such as natural, bypass and separation-induced transition. It has been used in varying applications such as helicopter blades (Sheng et al., 2016) and wind turbines (Sørensen, 2009). Despite its success, the $\gamma - Re_\theta$ model is not free from flaws, as it does not account for effects such as roughness or crossflow transition. Furthermore its formulation is not Galilean invariant, meaning that the application of the model if there are multiple moving walls is troublesome. Nonetheless, a few extensions to the model that remedy these deficiencies have been published (Langtry, 2015; Minot et al., 2017), and Galilean invariance has been addressed in the publication of the γ model (Menter et al., 2015), which is mostly a simplification of the $\gamma - Re_\theta$ model.

There are other transition models available in the literature which rely on different approaches. The Amplification Factor Transport (AFT) model (Coder and Maughmer, 2014; Coder, 2019) aims at replicating the framework of the e^N method but using a local formulation. It has mainly seen use in the aerospace community (Denison and Pulliam, 2018). Another notable example is the $k_T - k_L - \omega$ model (Walters and Cokljat, 2008), which is based on the concept of laminar kinetic energy, and attempts a more phenomenological description of the transition process. The separation between transition and turbulence models allows for the exploration of different coupling approaches (Medida and Baeder, 2011; Coder and Maughmer, 2015), and some algebraic transition models have also been proposed (Cakmakcioglu et al., 2018; Menter et al., 2022).

When considering naval applications, the main area of focus of transition has been in the simulation of model-scale propellers, with the $\gamma - Re_\theta$ and γ transition models being the most commonly used models. Nonetheless, one of the earliest examples of transition modelling for a propeller was done with the $k_T - k_L - \omega$ model (Wang and Walters, 2012). The effect of transition modelling with the $\gamma - Re_\theta$ model has been assessed by Bhattacharyya et al. (2015) which reported an improvement in their numerical predictions. A comparison between the results obtained with the $k - \omega$ SST model and the $\gamma - Re_\theta$ model at varying Reynolds numbers is presented in Baltazar et al. (2021). The influence of the inlet turbulence quantities is assessed in Baltazar et al. (2018), which shows that high values of the turbulence intensity and eddy-viscosity ratio are required to avoid an overprediction of laminar flow. Further work comparing velocity profiles for the laminar and turbulent regime on a propeller blade are discussed in Baltazar et al. (2020). The overprediction of laminar flow is also observed with the γ model, as detailed in Li et al. (2019). In Webster et al. (2019), the coupling between the γ model and a Reynolds-stress model is assess to predict propeller performance. The influence of transition on cavitation has also been discussed in Viitanen et al. (2019), Ge et al. (2021), Gaggero and Villa (2018), Gaggero (2022).

One of the issues that is common for all transition models proposed is the inability to account for crossflow transition. This is particularly important in the simulation of propellers, due to the strong three-dimensional nature of the boundary layer and the presence of adverse pressure gradients. Thus, it is then not surprising that the use of transition models without any sensitivity to crossflow leads to a too large extent of laminar flow. Some extensions for the inclusion of crossflow in the $\gamma - Re_\theta$ model have been proposed in Langtry (2015), Grabe et al. (2016), and one example of such application for marine propellers is given in Moran-Guerrero et al. (2018).

Most of the crossflow extensions proposed in the literature make use of the helicity (or streamwise vorticity), a quantity that uses the velocity vector in its definition, therefore making the extension not Galilean invariant. Other models, such as the one given in Rubino and Visonneau (2022), avoid using the helicity, but suffer from the same issue. This is particularly important for the simulation of propellers where the rotational motion of the propeller is usually prescribed using a body-fixed reference frame. Unless special care is taken, numerical simulations using such an approach with the $\gamma - Re_\theta$ model or any crossflow extensions that use the helicity with the γ model will result in incorrect applications of the models. The authors note that in the publications that fall under these scenarios, no mention was given regarding this issue and so it is unclear whether steps were taken to remedy this issue.

This work aims at exploring the influence and importance of crossflow modelling on the performance and flow field of a model-scale propeller in open water conditions. A controllable pitch propeller is used in this study, and simulations are performed for varying advance coefficients, to highlight the effects when the propeller is heavily or lightly loaded. The γ model (Menter et al., 2015) is selected as the transition model for the study since it is inherently Galilean invariant. Two alternative crossflow extensions are tested, the first being the default extension available in STARCCM+, while the second crossflow term is based on the work of Grabe et al. (2016). While both of the formulations rely on the helicity, their application is tailored to ensure that the velocity relative to the wall is used. The approach to ensure the correct application of the model is tested on the flow over a prolate spheroid and its results are used to highlight the importance of using the correct velocity in the crossflow term and also to verify that the employed approach works successfully. The influence of the turbulence quantities specified at the inlet is also addressed along with the effect of the roughness parameter required in one of the crossflow extensions. Baseline simulations without a crossflow term are performed as well.

The structure of the remainder of the paper is the following: Section 2 describes the mathematical formulation of the problem, including a description of the turbulence model, transition model and corresponding crossflow extensions. The problem definition and numerical settings are detailed in Section 3, while the results obtained for the prolate spheroid and the importance of Galilean invariance is given in Section 4. The results obtained for the propeller are presented and discussed in Section 5, and the main conclusions of this work are then summarized in Section 6.

2. Mathematical models

The work discussed in this paper deals with the flow of an incompressible Newtonian fluid. In all the simulations performed, the flow

can be considered as statistically steady, such that mean quantities represent a time average. Under these conditions, the Reynolds-averaged Navier–Stokes (RANS) equations can be written as

$$\frac{\partial U_i}{\partial x_i} = 0, \tag{1}$$

$$\rho U_j \frac{\partial U_i}{\partial x_j} = -\frac{\partial P}{\partial x_i} + \frac{\partial}{\partial x_j}\left[\mu\left(\frac{\partial U_i}{\partial x_j} + \frac{\partial U_j}{\partial x_i}\right)\right] + \frac{\partial \tau_{ij}}{\partial x_j}, \tag{2}$$

where U_i are the Cartesian components of the mean velocity vector, x_i are the coordinates of the Cartesian coordinate system, P is the mean pressure, relative to the hydrostatic, τ_{ij} is the Reynolds stress tensor and ρ and μ are the density and dynamic viscosity of the fluid, respectively.

The calculation of the Reynolds stresses is done following the eddy viscosity hypothesis of Boussinesq

$$\tau_{ij} = \mu_t\left(\frac{\partial U_i}{\partial x_j} + \frac{\partial U_j}{\partial x_i}\right) - \frac{2}{3}k\delta_{ij}, \tag{3}$$

in which μ_t is the eddy viscosity and k is the turbulence kinetic energy.

The system of equations is closed with the $k-\omega$ Shear Stress Transport (SST) model (Menter, 1994). The model has two transport equations, one for k and another for the specific turbulence dissipation rate ω. The equation for k is written as

$$\rho U_j \frac{\partial k}{\partial x_j} = \mu_t S^2 - \rho\beta^*\omega k + \frac{\partial}{\partial x_j}\left[\left(\mu + \sigma_k\mu_t\right)\frac{\partial k}{\partial x_j}\right], \tag{4}$$

where S is the mean strain-rate magnitude and β^* and σ_k are constants. The equation for ω is

$$\rho U_j \frac{\partial \omega}{\partial x_j} = P_\omega - \beta\omega^2 + \frac{\partial}{\partial x_j}\left[\left(\mu + \sigma_\omega\mu_t\right)\frac{\partial \omega}{\partial x_j}\right] + 2\left(1-F_1\right)\frac{\rho\sigma_{\omega 2}}{\omega}\frac{\partial k}{\partial x_j}\frac{\partial \omega}{\partial x_j}, \tag{5}$$

in which β, σ_ω and $\sigma_{\omega 2}$ are constants and F_1 is a blending function of the model, responsible for switching between the $k-\epsilon$ formulation in the freestream to the $k-\omega$ formulation inside the boundary-layer. The implementation of the $k-\omega$ SST model used in this work is described in Menter (1994) with two exceptions. The first is made evident in Eq. (4) and concerns the production term of k, which does not include a limiter. The second difference lies in the calculation of the eddy viscosity, which is computed as

$$\mu_t = \rho k \min\left(\frac{1}{\max\left(\omega, \left(SF_2\right)/0.31\right)}, \frac{0.6}{\sqrt{3}S}\right), \tag{6}$$

in which F_2 is another blending function of the SST model. This expression for the eddy viscosity includes an additional limiter when compared to the definition present in Menter (1994), which aims at preventing high values of μ_t in stagnation regions, since the production of k is not limited. It is noted that these subtle changes in the formulation of the SST model can have an impact on the solution, especially when transition models are employed (Minot et al., 2015; Langel et al., 2016; Venkatachari et al., 2021; Lopes et al., 2022b).

The transition model used in this work is the γ model by Menter et al. (2015). As stated previously, this model is a simplification of the $\gamma - Re_\theta$ model (Langtry and Menter, 2009), and it includes a single transport equation for the intermittency γ. The intermittency is defined as the fraction of time in which a given point in the domain is turbulent, with values of approximately 0 representing laminar flow, and values of 1 corresponding to fully turbulent flow. The transport equation for γ is

$$\rho U_j \frac{\partial \gamma}{\partial x_j} = P_\gamma - D_\gamma + \frac{\partial}{\partial x_j}\left[\left(\mu + \frac{\mu_t}{\sigma_\gamma}\right)\frac{\partial \gamma}{\partial x_j}\right], \tag{7}$$

where P_γ and D_γ are the production and destruction terms of γ, respectively, and σ_γ is a constant. The production term P_γ is defined as

$$P_\gamma = \rho S F_{length} F_{onset} \gamma\left(1-\gamma\right), \tag{8}$$

where F_{length} is a constant and F_{onset} is a function responsible for triggering the onset of transition. The remainder of the formulation of the γ model, and its coupling with the $k-\omega$ SST model can be found in Menter et al. (2015).

Two different crossflow extensions are considered in this paper, both based on the helicity of the flow. The first corresponds to the term available in STAR-CCM+, modifying the F_{onset} function in Eq. (8) to be

$$F_{onset} = \max\left(F_{onset,orig}, F_{onset,SCF}\right), \tag{9}$$

where $F_{onset,orig}$ is the original formulation of F_{onset} used in the γ model, and $F_{onset,SCF}$ corresponds to a function that triggers the onset of transition based on crossflow transition. It is written as

$$F_{onset,SCF} = \min\left[\max\left(f_{SCF} - 1, 0\right), 1\right], \tag{10}$$

in which f_{SCF} is the cross-flow function calculated as

$$f_{SCF} = \frac{C_r \Delta H_{SCF} Re_{\theta c}}{\left(Re^*_{\delta 2t}\right)_{tr}}. \tag{11}$$

In Eq. (11), C_r is the surface roughness constant, ΔH_{SCF} is the dimensionless crossflow strength, $Re_{\theta c}$ is the critical momentum thickness Reynolds number that is used in the γ model and $\left(Re^*_{\delta 2t}\right)_{tr}$ is the critical crossflow displacement thickness Reynolds number. The surface roughness constant represents the effect of roughness on crossflow and is obtained through

$$C_r = 2 - 0.5^{\frac{h}{0.25\times 10^{-6}}}, \tag{12}$$

where h is the crossflow inducing roughness height.

The dimensionless crossflow strength is defined as

$$\Delta H_{SCF} = H_{SCF}\left[1 + \min\left(\frac{\mu_t}{\mu}, 0.4\right)\right], \tag{13}$$

where

$$H_{SCF} = \frac{He}{|U_i|^2}d, \tag{14}$$

in which d is the nearest wall distance, $|U_i|$ is the magnitude of the mean velocity and He is the helicity defined as

$$He = \left|U_i W_i\right|, \tag{15}$$

where W_i is the mean vorticity vector.

The critical crossflow displacement thickness Reynolds number is estimated from Arnal's C1 criterion (Arnal et al., 1984)

$$Re^*_{\delta 2t} = \begin{cases} \frac{300}{\pi}\arctan\left[\frac{0.106}{(H-2.3)^{2.05}}\right] & , \quad 2.3 \le H < 2.7 \\ 150 & , \quad H < 2.3 \end{cases} \tag{16}$$

in which H is the shape factor computed as

$$H = 2 + 4.14l - 83.5l^2 + 854l^3 - 3337l^4 + 4576l^5, \tag{17}$$

where

$$l = 0.25 - \lambda_{\theta L}, \tag{18}$$

in which $\lambda_{\theta L}$ is the pressure gradient parameter used in the formulation of the γ model.

The second crossflow extension used in this paper is based on the work of Grabe et al. (2016). Although initially developed for the $\gamma - Re_\theta$ model, it has been combined with the γ model as described in Lopes et al. (2022a). In this approach, P_γ is written as

$$P_\gamma = \left(F_{length} F_{onset} + F_{length,CF} F_{onset,CF}\right)\rho S\gamma\left(1-\gamma\right), \tag{19}$$

in which $F_{length,CF}$ is a constant and $F_{onset,CF}$ is the transition onset function based on crossflow transition. The calculation of $F_{onset,CF}$ employs a structure of auxiliary functions similar to those used for F_{onset} in the original formulation of the γ model, with

$$F_{onset,CF} = \max\left(F_{onset2,CF} - F_{onset3,CF}, 0.0\right), \tag{20}$$

$$F_{onset3,CF} = \max\left(1 - \left(\frac{R_T}{2}\right)^3, 0.0\right), \tag{21}$$

$$F_{onset2,CF} = \min\left(\max\left(F_{onset1,CF}, F^4_{onset1,CF}\right), 2.0\right), \tag{22}$$

$$F_{onset1,CF} = \frac{Re_{He}}{0.7Re^+_{He,t}}. \tag{23}$$

This group of functions follows a similar structure to those in the formulation of the γ model. R_T is the turbulent Reynolds number, $Re^+_{He,t}$ is the Helicity Reynolds number at transition onset, and Re_{He} is the local Helicity Reynolds number. The latter is computed as

$$Re_{He} = \frac{\rho d^2}{\mu}\frac{He}{U}. \tag{24}$$

The Helicity Reynolds number at transition onset is estimated from

$$Re^+_{He,t} = \max\left(-456.83\, H^+_{12} + 1332.7, 150.0\right), \tag{25}$$

where H^+_{12} is an estimate of the shape factor

$$H^+_{12} = 4.02923 - \left(-8838.4\lambda^{+4} + 1105.1\lambda^{+3} - 67.962\lambda^{+2} + 17.574\lambda^+ + 2.0593\right)^{0.5}. \tag{26}$$

The pressure gradient parameter λ^+ is given by

$$\lambda^+ = \frac{\rho l^2}{\mu}\frac{dU_e}{ds}, \tag{27}$$

where

$$l = \frac{1}{C_{He,max}}\frac{2}{15}d, \tag{28}$$

with $C_{He,max} = 0.6944$.

The quantity $\frac{dU_e}{ds}$ is the streamwise derivative of the velocity at the edge of the boundary layer, U_e, calculated from

$$\frac{dU_e}{ds} = \frac{U_i}{U}\frac{dU_e}{dx_i}, \tag{29}$$

where a relationship between the velocity and pressure derivatives is established through Bernoulli's equation

$$\frac{\partial U_e}{\partial x_i} = -\frac{1}{\rho U_e}\frac{\partial p}{\partial x_i}. \tag{30}$$

Finally, U_e is estimated locally from

$$U_e = \sqrt{V^2_\infty + \frac{p_\infty - p}{\frac{1}{2}\rho}}. \tag{31}$$

3. Numerical setup

The flow solver used in this work is the commercial software STAR-CCM+ 2022.1.1. It uses the finite volume method to discretize the differential equations and a segregated solver is employed to solve the transport equations. The SIMPLE algorithm is used to address the pressure–velocity coupling and second order schemes are used for the discretization of the convective term of each transport equation.

The main geometry considered in this work is a four bladed controllable pitch propeller in an open water setup at model scale. The Reynolds number of the flow, based on the chord length and velocity at 70% of the propeller radius, ranges from 7.5×10^5 to 8×10^5, and the advance coefficient J is varied from 0.34 to 0.992. The advance coefficient is defined as

$$J = \frac{V_A}{nD}, \tag{32}$$

where V_A is the advance velocity, n is the propeller rotation rate in rps and D is the diameter of the propeller. The change in the advance coefficient is done mainly by keeping the propeller rotation rate constant and modifying the velocity at the inlet. Table 1 presents the main particulars of the propeller geometry.

Table 1
Main particulars of the propeller used in the study.

Characteristic	Symbol	Value
Propeller diameter	D [m]	0.21
Chord length	$c_{0.7R}$ [m]	0.0468
Number of blades	Z	4
Pitch ratio	$P/D_{0.7R}$	0.978
Blade area ratio	A_E/A_0	0.376

The propeller is placed in the centre of the computational domain which is a cylinder with a diameter of $60D$ where D is the diameter of the propeller. The inlet and outlet are placed $30D$ away from the propeller plane. The domain is divided into two regions: one inner region around in the propeller in a cylindrical shape, and another outer region which comprises the rest of the domain. The inner region has a length of $2D$ and a diameter of $1.25D$, and it is centred on the propeller plane. In this region, the equations are solved in the body-fixed coordinate system that rotates with the propeller, such that the flow can be considered as steady. The advance velocity, turbulence intensity and turbulent viscosity ratio are specified at the inlet, whereas the pressure is set at the outlet.

The specification of the turbulence quantities at the inlet is of extreme importance in simulations with transition models, since they strongly influence the location of transition. Throughout this study, most of the simulations are carried out using a value of 1% for the inlet turbulence intensity I and 1.0 for the eddy viscosity ratio μ_t/μ. Although these are significantly lower than what is observed for the simulation of model scale propellers (Baltazar et al., 2018), it is noted that the γ model relies strongly on these values to start transition, but the crossflow terms are not expected to be as influenced by them. Regardless, their impact on crossflow transition is also assessed throughout the paper, with simulations using a value of $I = 3\%$ and $\mu_t/\mu = 500$. We acknowledge the latter to be physically questionable, but it is required to prevent the decay of k from the inlet to the propeller blade, in the absence of any other approach to deal with the decay of freestream turbulence.

Another parameter that can have some influence is the roughness height h in Eq. (12), which is a user input. It is noted that due to its formulation, C_R can range between 1 and 2, with the higher value promoting transition earlier. The default value for h in STAR-CCM+ is 3×10^{-6}, which results in a value for C_R of approximately 2. A sensitivity study is conducted for the influence of this parameter, for values of h that correspond to C_R ranging from 1 to 2. Nonetheless, most of the simulations performed in this study use the default value of h, unless otherwise stated.

In order to distinguish between the different crossflow extensions used in this work the following terminology is followed:

- The simulations performed without any crossflow term are identified as being done with the γ model, or without crossflow;
- The calculations using the default crossflow term in STAR-CCM+, corresponding to that described in Eqs. (9) through (18) is referred to as $CF1$;
- The formulation by Grabe et al. (2016), described in Eqs. (19) up to (31) is defined as $CF2$.

A set of five grids is generated and used for all the simulations. Since the grids are unstructured, it is impossible to make them geometrically similar. Nonetheless, all target sizes are set to lead to a specified refinement ratio, with the same applying for the stretching ratio and number of layers in the prism layer, following the procedure described in Crepier (2017). The total thickness of the prism layer is set so that $y^+_{max} < 1$ for the coarsest grid. Details of the grid set are given in Table 2.

Table 2
Details of the grids used for the simulations in terms of the number of faces on the propeller blades $\#S$, total number of volume cells $\#V$, design refinement ratio $(h_i/h_1)_{design}$ and actual refinement ratio $(h_i/h_1)_{actual}$.

Grid	$\#S$	$\#V$	$(h_i/h_1)_{design}$	$(h_i/h_1)_{actual}$
5	75,056	6.8M	2.0	1.77
4	109,576	12.4M	1.67	1.46
3	146,914	20.7M	1.33	1.26
2	192,017	31.7M	1.14	1.10
1	234,168	45.8M	1.0	1.0

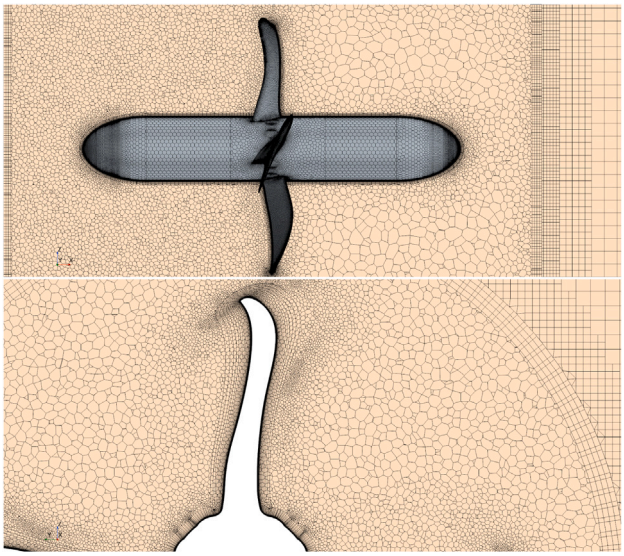

Fig. 1. Grid topology around the propeller blades for the coarsest grid.

The cell type used in the grids varies from one region to another. Polyhedral cells are used in the inner region that contains the propeller, enabling the use of the advancing layer mesher, which allows for a high quality prism layer around the propeller blades. The outer region is meshed using hexahedral cells, which expand from the interface between the two regions to the outer boundaries of the computational domain. The coarsest grid is illustrated in Fig. 1.

The five grids are used in order to estimate the numerical uncertainty of the selected quantities of interest, following the procedure developed by Eça & Hoekstra (Eça and Hoekstra, 2014). The method assumes a power series expansion of the discretization error e as

$$e \approx \phi_i - \phi_0 = \alpha h_i^p, \tag{33}$$

in which ϕ_i is the value of a local or integral quantity obtained in grid i, ϕ_0 is the estimate of the exact solution for that quantity, α is the error constant, h_i is the typical cell size spacing and p is the observed order of grid convergence. Eq. (33) has three unknowns in the form of ϕ_0, α and p, so solutions from three grids would be enough to obtain the discretization error. However, in order to handle the noise typically present in CFD simulations, Eq. (33) is solved in the least-squares sense, and hence more than three grids are required. The estimation of the numerical uncertainty for a given grid then relies on the quality of the fit, the estimate of the discretization error for that grid and the variation of the solution across different grids.

For the estimation of the discretization error to be meaningful, it must be assured that this is the dominant contribution to the numerical error. In steady simulations the numerical error is typically assumed to have three contributions (Roache, 1998): round-off error, iterative error and discretization error. The round-off error is caused by the finite precision in which computers and machines operate. The iterative error arises from several aspects of the solution procedure such as the linearization of the equations and the iterative methods used to solve the linear system of equations.

The round-off error is assumed to be negligible compared to the remaining components of the numerical error as the double-precision version of STAR-CCM+ is used in this work. Regarding the iterative error, it is monitored through the convergence of the forces with each iteration and through the evolution of the dimensionless residuals in the L_2 and L_∞ norm. The residuals are normalized such that they correspond to dimensionless variables changes in a simple Jacobi iteration.

The main quantities of interest in this study are the thrust and torque coefficients, K_T and K_Q respectively, obtained by

$$K_T = \frac{T}{\rho n^2 D^4}, \tag{34}$$

$$K_Q = \frac{Q}{\rho n^2 D^5}, \tag{35}$$

where T and Q are the thrust and torque of the propeller, respectively. The efficiency of the propeller η, obtained from K_T and K_Q is also evaluated

$$\eta = \frac{K_T}{K_Q}\frac{J}{2\pi}. \tag{36}$$

In terms of local quantities, we consider the skin-friction coefficient C_f and the pressure coefficient C_p, defined as

$$C_f = \frac{\tau_w}{\frac{1}{2}\rho V_{ref}^2}, \tag{37}$$

$$C_p = \frac{P - P_{ref}}{\frac{1}{2}\rho V_{ref}^2}. \tag{38}$$

In these equations, τ_w is the shear stress at the wall, P_{Ref} is the reference pressure, which corresponds to the pressure at the outlet and V_{ref} is the reference velocity, taken as the velocity as 70% of the propeller radius, given by

$$V_{ref} = \sqrt{V_A^2 + (0.7\pi n D)^2}. \tag{39}$$

4. Importance of Galilean invariance

This section discusses the preliminary computations done for the 6:1 prolate spheroid. This geometry was used to test the implementation of the crossflow terms, and is presented here to show the importance of said implementation. The Reynolds number of the flow is 6.5×10^6, and the spheroid has an inclination of 10° relative to the incoming flow. The spheroid is placed in the centre of a cube of side $20L$, where L is the length of the spheroid. However, the computational domain consists of half of the cube, with a symmetry plane at the centreline of the spheroid. The inlet and outlet boundaries are approximately $19.5L$ away from the spheroid. A single grid with 15.6M cells was generated and used for the simulations. A coarser grid was initially used, but the results were found to be strongly influenced by the numerical error. This is not surprising, as the γ transition model has been shown to be significantly affected by the grid quality and resolution in some cases (Lopes et al., 2021; Zastawny and Lardeau, 2022).

The simulations are performed considering two different numerical setups. The first setup, hereby designated as the normal setup, specifies the velocity directly at the inlet. In the second setup, named as MRF, the velocity is split into two parts. The first part corresponds to 10% of the velocity, and it is set at the inlet. The second part corresponds to the remaining 90%, and it is set as the velocity of the reference frame. This intends to mimic the procedure usually employed when the Moving Reference Frame approach is used for propeller simulations.

From a physical standpoint, the two setups represent the same problem and flow condition, but from a numerical point of view they do not, and as such, models that are not Galilean invariant will produce different solutions. It is also noted that the specification of the

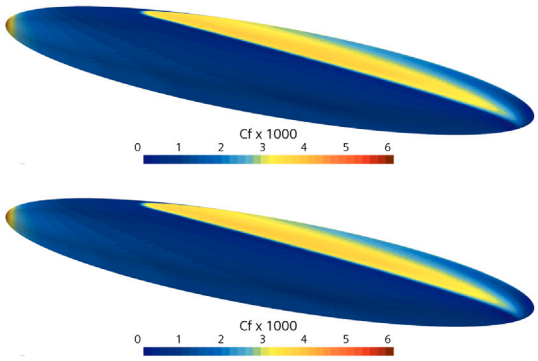

Fig. 2. Skin-friction coefficient obtained on the surface of the prolate spheroid with the γ model without a crossflow term on the normal setup (top) and on the MRF setup (bottom). The flow direction is from left to right.

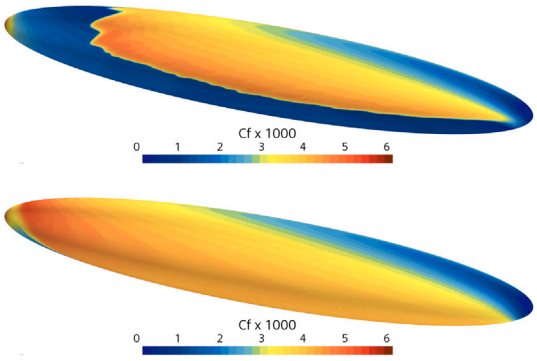

Fig. 3. Skin-friction coefficient obtained on the surface of the prolate spheroid with the γ model with $CF1$ on the normal setup (top) and on the MRF setup (bottom). The flow direction is from left to right.

turbulence quantities at the inlet was done directly through the values of the turbulence kinetic energy and the specific dissipation rate. If the turbulence intensity and turbulent viscosity ratio are used instead, the boundary conditions would change depending on the setup, which is not the intended scenario. Nonetheless, the values set for k and ω correspond to turbulence intensity and turbulent-viscosity ratio of 1% and 0.195, respectively, when considering the normal setup.

The first comparison between the solution obtained on the two setups is done for the γ model, which is known to be Galilean invariant. The skin-friction coefficient obtained on both simulations is shown in Fig. 2, and the comparison between the two simulations shows the solution to be the same. Since the γ model is Galilean invariant, this is not a surprising result, and it confirms that the two setups are indeed representative of the same physical problem.

The same exercise is now repeated but with the default crossflow term available in STAR-CCM+ turned on. The C_f distribution on the surface of the spheroid for the two setups is illustrated in Fig. 3, and clear differences are observed between the simulations. The simulation obtained with the normal setup represents the typical solution observed for this test case, in good agreement with other results using crossflow extensions (Lopes et al., 2022a), although the formulations are not the same. There is a significant increase of the turbulent flow region when crossflow is activated. More importantly however, there is no match between the two setups, and the simulation obtained with the MRF setup resembles that of a fully turbulent flow, with a small extent of laminar flow near the leading edge of the spheroid. The premature transition and difference between the simulations can be traced back to the helicity, a key quantity in the crossflow term, which exhibits different values in the incoming flow region right upstream of the spheroid. The lack of Galilean invariance is tied to the calculation of the helicity, which requires the local flow velocity, a quantity that is directly affected by the setup used for the simulation. Ultimately, this shows that the direct use of a crossflow term that uses the helicity results in an incorrect application of the model if the flow velocity is set through motion of the reference frame. In order to ensure a proper application of the crossflow extension and the computation of the helicity, the velocity relative to the wall must be used.

In order to apply the crossflow terms correctly when a moving reference frame is used, modifications are required. It is not possible to modify the equation of the transition model directly in STAR-CCM+, although it is possible to add source terms to the equations of the turbulence model, which is the way used to make the correction. First, the model for passive scalars is turned on, and an equation for a passive scalar is constructed with the corresponding convection, diffusion and source terms such that it represents the transport equation of γ, with the exception that the helicity is computed using the velocity relative to the wall. Then, source terms are added to the equations of the turbulence model, using the passive scalar variable which represents the correct γ, in order to properly account for the effect of the transition model on the turbulence model. It is also mentioned that the transition model as implemented in STAR-CCM+ is active and used nonetheless, as this enables some field functions that make the reproduction of the γ equation simpler and easier. Although this results in a slightly higher computational cost, due to the solution of one additional transport equation, we consider the cost to be small when compared to the benefits when setting up the corrected equation. As an additional consequence, the source term that is added to the transport equation for k must cancel out the wrong implementation of the transition model, and then introduce the terms that correspond to the corrected one.

The application of this method to the prolate spheroid test case results in a match between the two simulations setups, as exhibited in Fig. 4. The evolution of the flow around the surface of the spheroid in both setups shows a good match with the previously obtained solution with the original implementation of the model in the normal setup, which is considered as the reference and correct solution. This shows that the correction of the helicity and the approach to properly apply the crossflow extension is working successfully. It is however noted that there is a slight difference in the solution obtained between the two different implementations of the transition model with the crossflow term regarding the location of the transition region, near the symmetry plane at the upper side of the spheroid. Although the cause for this difference could not be exactly found, it is believed that it is an influence of the numerical error on the simulation, that still persists at the current refinement level. Regardless, the good overall match between the setups provides sufficient confidence to use this approach for the propeller simulations, especially when considering the issues demonstrated if the default implementation of the crossflow term is used.

The second crossflow extension used in this work is not available in STAR-CCM+ and had to be implemented through field functions and the reconstructed γ transition equation. Although there is no reference solution for that model, a similar check was conducted to ensure that the normal and MRF setups produced the same solution. This was confirmed, as the two setups did not exhibit any significant changes. Unless otherwise stated, all remaining simulations performed throughout the remainder of the paper use the correct calculation of the helicity.

It should be pointed out that for the purposes of the present study the use of the velocity relative to the wall is a solution to the lack of Galilean invariance of the crossflow terms since all the walls in the computational domain have the same motion. This holds true for the prolate spheroid and for the propeller in open water conditions. However the applicability of this approach would be questionable when there are walls in the domain that have different motions relative to one

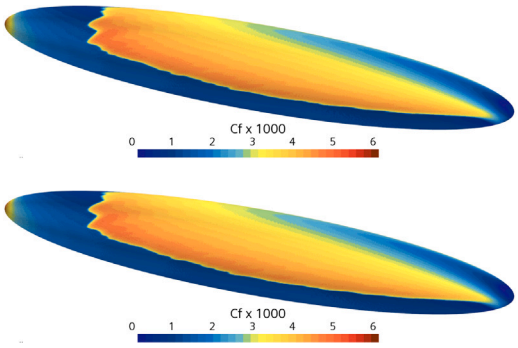

Fig. 4. Skin-friction coefficient obtained on the surface of the prolate spheroid with the γ model and the corrected $CF1$ term on the normal setup (top) and on the MRF setup (bottom). The flow direction is from left to right.

another, such as a propeller in-behind or a ducted propeller. In these cases it would not be clear what velocity to use in the areas of the domain that lie in close vicinity of walls with different motions, such as the region between the blade tip and the duct, and a Galilean invariant formulation would be required. Nonetheless, the present approach is sufficient for the simpler case of a propeller in open water.

5. Results

Having completed the discussion of the results obtained for the prolate spheroid and gained confidence regarding the approach to correctly incorporate the crossflow extensions in the simulations, focus is now given to the propeller simulations. As a starting point, the discussion begins by addressing the iterative convergence of the simulations. Fig. 5 illustrates the convergence of the L_∞ norm of the residuals for two simulations performed on the finest grid, one without any crossflow extension, and another with CF1. Both cases show trends typical of simulations done with transition models, which are the strong oscillation of the residuals with the iterations, the high residual obtained for the intermittency and residual stagnation. The comparison between the two cases show that lower residuals are obtained when the crossflow term is used, with the exception of the residual of γ. Although Fig. 5 only concerns a single case, the trends are representative of those observed through the range of advance coefficients computed, and are also valid for both crossflow terms. We note that while the residual for the intermittency is high, this is a behaviour observed in simulations that use intermittency-based models, in particular those that are part of the Local Correlation-based Transition Modelling approach such as the $\gamma - Re_\theta$ or γ models. Furthermore, Fig. 5 displays the L_∞ norm of the residual, which corresponds to the maximum residual of each variable observed in the entire computational domain. This is a conservative measure of the residuals, which are often given in the L_2 norm. For this case, the L_2 norm of the intermittency residual would be of the order of magnitude of 10^{-3}, which would correspond to a much more reasonable level. For the same reason, the residuals of the remaining variables would also be around two orders of magnitude lower when given in the L_2 norm. Besides the residuals, the evolution of the thrust and torque coefficients was also monitored and no significant variation with the iterations was observed when the simulations were completed.

Another point of interest is the numerical uncertainty arising from the discretization error. Tables 3 and 4 present the estimated uncertainty for the thrust and torque coefficients at different advance coefficients, respectively, for the simulations performed without a crossflow term, and those done with $CF1$ and $CF2$. The comparison across the different modelling approaches shows that the use of a crossflow term tends to lead to an increase of the uncertainty when compared to the simulations done without crossflow, although there are no significant differences between the two crossflow terms. This indicates that changes in the flow field are likely to be responsible by the change in the uncertainty. Some trends are common across all models, like the increase of the uncertainty with the increase of the advance coefficient. Furthermore, in general, the uncertainty estimated for K_Q is higher than that of K_T.

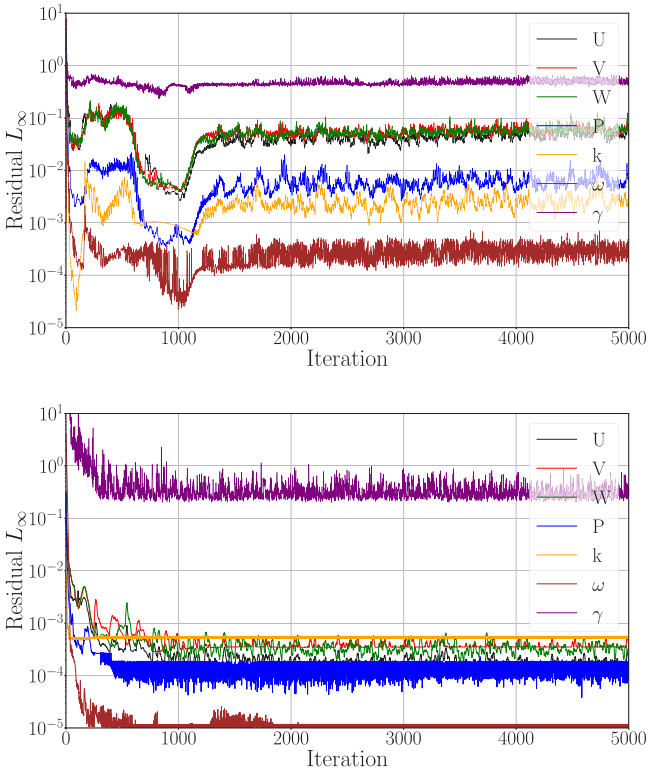

Fig. 5. Evolution of the L_∞ norm of the residuals for a simulation on the finest grid without crossflow (top) and with the $CF1$ crossflow extension (bottom) for $J = 0.751$.

Table 3
Estimate of the numerical uncertainty obtained for the thrust coefficient on the finest grid for varying advance coefficients and different crossflow terms.

J	$U(K_T)$		
	γ	$\gamma + CF1$	$\gamma + CF2$
0.34	2.2%	1.3%	0.4%
0.425	1.6%	1.7%	0.9%
0.508	0.9%	2.9%	2.5%
0.588	1.5%	2.2%	3.5%
0.67	2.1%	4.8%	4.4%
0.751	2.1%	5.9%	5.9%
0.835	4.4%	7.8%	10.7%
0.914	4.7%	8.3%	22.7%
0.992	35.1%	22.3%	45.3%

Table 4
Estimate of the numerical uncertainty obtained for the torque coefficient on the finest grid for varying advance coefficients and different crossflow terms.

J	$U(K_Q)$		
	γ	$\gamma + CF1$	$\gamma + CF2$
0.34	4.3%	5.2%	1.3%
0.425	3.5%	3.9%	1.7%
0.508	1.7%	6.5%	4.0%
0.588	1.9%	5.5%	5.0%
0.67	3.4%	8.8%	5.1%
0.751	3.3%	10.7%	7.0%
0.835	9.5%	12.4%	11.8%
0.914	8.6%	15.9%	18.9%
0.992	27.3%	22.0%	54.9%

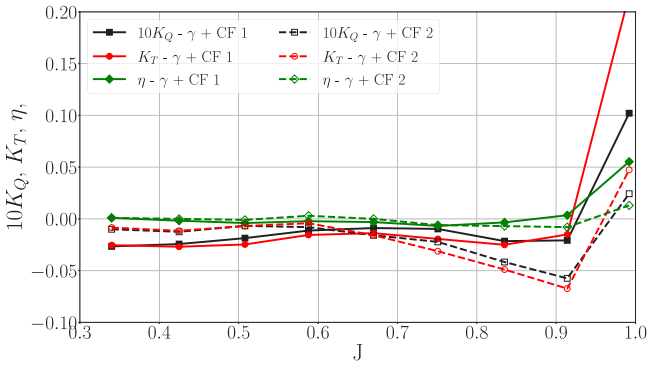

Fig. 6. Relative variation of K_T, K_Q and η with the advance coefficient for the two crossflow extensions relative to the simulations without crossflow.

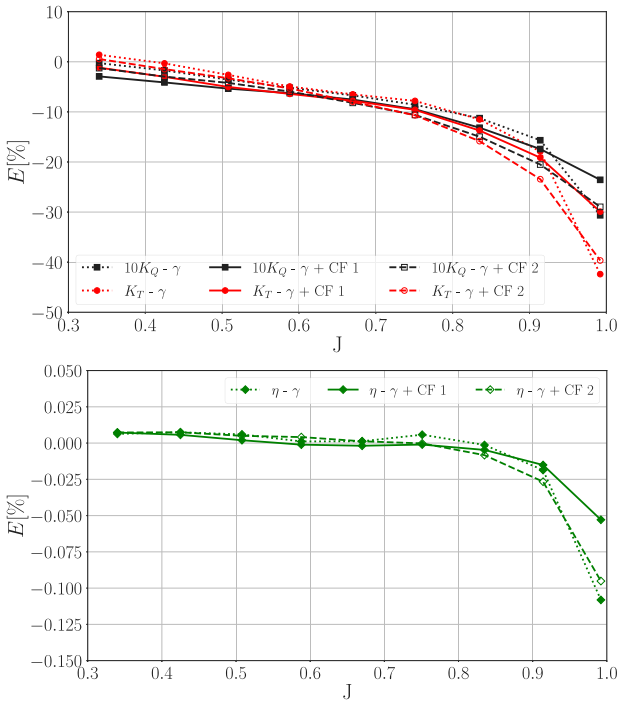

Fig. 7. Relative comparison error of K_T, K_Q (top) and comparison error of η (bottom) for varying advance coefficient with available experimental results for the simulations without crossflow and the two crossflow modelling terms.

While the estimated numerical uncertainty may appear to be high, it is normal to expect higher uncertainty than what is typically observed for fully turbulent simulations. This is due to the fact that the transition region is an area of high gradients where the mesh is not as fine as the leading or trailing edges, since its location is not known when the grid is generated. We have looked at the C_f distribution on the surface of the blades for the different grids and found that differences in the flow field were only noticeable on the coarsest grid, and when the crossflow term is not used. For the remaining cases, the effect of grid refinement was found to be barely visible, and even less so when the coarsest grid was not considered. The results presented in the remainder of this paper correspond to those obtained in the finest grid.

Addressing the performance of the propeller, Fig. 6 illustrates the thrust and torque coefficients, and the efficiency obtained for the simulations with the two crossflow terms, given relative to the simulations without crossflow, for each advance coefficient. It is noted that while this may be an unconventional way of presenting the data, it enables for a better comparison than the open-water diagram since the data for the propeller is proprietary and cannot be given. The results presented in Fig. 6 show that, with the exception of the highest advance coefficient tested, the inclusion of crossflow transition leads to a reduction in K_T and K_Q, regardless of the term used. On the other hand, the efficiency does not exhibit a clear trend, although its change is much smaller than that of K_T and K_Q.

When comparing the two different crossflow terms, it is observed that different behaviours are obtained at low and high advance coefficients. For the lower advance coefficients, the thrust and torque obtained with the $CF1$ model are lower than that of $CF2$. As a matter of fact, the difference between the two crossflow terms in these quantities is larger than the difference between $CF2$ and the baseline solutions without a transition model. As the advance coefficient is increased up to $J = 0.588$, the differences to the baseline solution decrease for both crossflow terms. Further increasing the advance coefficient leads to a decrease in thrust and torque. However, this effect is stronger for $CF2$, so that for $J > 0.6$, the thrust and torque obtained with $CF2$ are now lower than those obtained with $CF1$, unlike what happened at the lower range of the advance coefficient calculated. In particular, the thrust coefficient obtained for $CF2$ at $J = 0.835$ is almost 5% lower than that of the baseline solution.

It must be mentioned that while Fig. 6 shows the total thrust and torque coefficients, the contributions of friction and pressure have been analysed separately. As expected, the pressure component is dominant when compared to the friction component, and the inclusion of crossflow effects causes an increase in the magnitude of the friction component, which in term leads to a slight increase in torque, and a decrease in thrust. This also means that while the effects of crossflow transition are naturally evident in the wall shear stress, the overall influence on the propeller performance ultimately comes from the changes in the pressure component.

The comparison error, E, of the thrust and torque coefficients and of the propeller efficiency are shown in Fig. 7. It is given as a percentage of the experimental value for K_T and K_Q, whereas for the efficiency it corresponds simply to the difference between the numerical results and the measurements. With the exception of the lowest advance coefficient, the numerical results underpredict both K_T and K_Q, with the differences being the largest when the propeller is either heavily or lightly loaded. For the highest advance coefficients, the underprediction of the thrust is more pronounced than that of the torque coefficient, causing the efficiency obtained in the simulations to be lower than the one measured experimentally. For the remaining conditions, the underprediction of the torque is slightly stronger, leading to a small overprediction of the efficiency. The three modelling approaches exhibit slight differences between each other, but not significant to the point of one providing a much better agreement with the experiments, indicating that the discrepancy is unlikely to be related to transition modelling. In this regard, it must be mentioned that the numerical setup does not attempt to reproduce the experimental arrangement. In particular, the experiments were performed in a cavitation tunnel where the shaft is located upstream of the propeller, influencing the inflow to the propeller. Furthermore, the velocity in the tunnel is measured downstream of the propeller, and a correction is applied to it in order to obtain the corresponding advance velocity. These factors will naturally influence the comparison between the measurements and the numerical results, meaning that a possible mismatch in the conditions is likely to be the dominant factor in the differences observed.

Fig. 8 presents the limiting streamlines and the skin-friction coefficient on the suction side of the propeller blades at $J = 0.425$ for the three crossflow modelling approaches. The limiting streamlines on the surface of the blade correspond to the direction of the wall shear stress vector. The transition from laminar to turbulent flow is evidenced by the quick increase in C_f downstream of the leading edge, and also by the change in the orientation of the streamlines. When the simulations are performed without a transition model, the flow is nearly fully laminar, with the occurrence of transition limited to a small

region near the tip of the blade. This is not unexpected, considering the low values set for the quantities of the turbulence model. Due to the absence of turbulent flow, there is also a significant region of separated flow near the trailing edge of the blade. When a crossflow term is included, the flow field on the propeller blade changes considerably, with a strong decrease of the size of the separated flow region. This is caused by the transition to turbulence that is no longer limited to the region near the tip of the blade but extends to around 60% of the radius of the propeller, with the location of transition occurring closer to the trailing edge as the distance to the root of the blade decreases. Near the root, the flow is nearly fully laminar, similarly to that observed for the simulation without crossflow. Since the conditions for the simulations are the same, it stands that the differences observed between the different cases are simply due to crossflow transition.

There is a visible difference between the two crossflow terms, as the solution obtained with $CF1$ exhibits earlier transition than $CF2$ and consequently a larger extent of turbulent flow. However, the difference does not seem large enough to justify the differences in K_T and K_Q discussed previously. In order to provide further clarification, we also consider the flow on the pressure side of the blade, illustrated in Fig. 9. In this case, the simulation without crossflow and the one with $CF2$ result in fully laminar flow, with a small region of separated flow at the trailing edge of the blade. On the other hand, the simulation performed with $CF1$ shows transition to take place at around 80% of the chord for almost the entire blade, which prevents flow separation. We recall that for this advance coefficient, the difference in K_T and K_Q between $CF1$ and $CF2$ were larger than those between $CF2$ and the simulation without crossflow, with the results from $CF1$ exhibiting the lowest thrust and torque. Considering the similarity in the flow field obtained with the two crossflow models on the pressure, it seems that the difference in the performance stems from prediction of transition on the pressure side, and the corresponding absence of flow separation. It is also noted that between $CF1$ and $CF2$, for this advance coefficient, it is the former that exhibits the most differences when compared to the simulation without crossflow, both in terms of the flow regime on the blade and in terms of the propeller performance.

The behaviour of the flow observed for the pressure and suction sides of the blade also explains the trends observed regarding the iterative convergence and the estimated numerical uncertainty of K_T and K_Q. Regarding the iterative convergence, the inclusion of crossflow effects prevents flow separation from taking place, resulting in a more stable flow configuration, and a better agreement with the steady flow assumption. It is then natural to expect that the simulations with crossflow exhibit better iterative convergence. On the other hand, the calculations performed without crossflow typically exhibit flow transition to take place either near the leading edge, or not at all. On the other hand, when a crossflow term is used, transition to turbulence can occur even at mid-chord, a region that is not as fine as the leading edge. As a consequence, the high gradients that occur in the transition region will naturally lead to higher numerical error.

The pressure coefficient on the suction side of the blade is shown in Fig. 10. It is observed that the pressure coefficient exhibits a smoother behaviour near the trailing edge when crossflow is included, as a consequence of the absence of flow separation. This leads to a slight local increase of C_p on the pressure side of the blade, along the trailing edge. Although it is not shown, a similar effect also takes place on the suction side of the blade, although it is not as noticeable as on the pressure side. Recalling that the differences in the torque and thrust for this advance coefficient were lower than 5%, it is expected that only small changes in the pressure coefficient are observed.

The remarks previously presented are valid for the cases at the low J range. With an increase of the advance coefficient, transition tends to move towards the trailing edge and or disappear on the suction side, whereas it begins to occur earlier in the pressure side. We now consider a condition where the propeller is lightly loaded ($J = 0.835$) and address first the suction side of the propeller blade, with C_f displayed

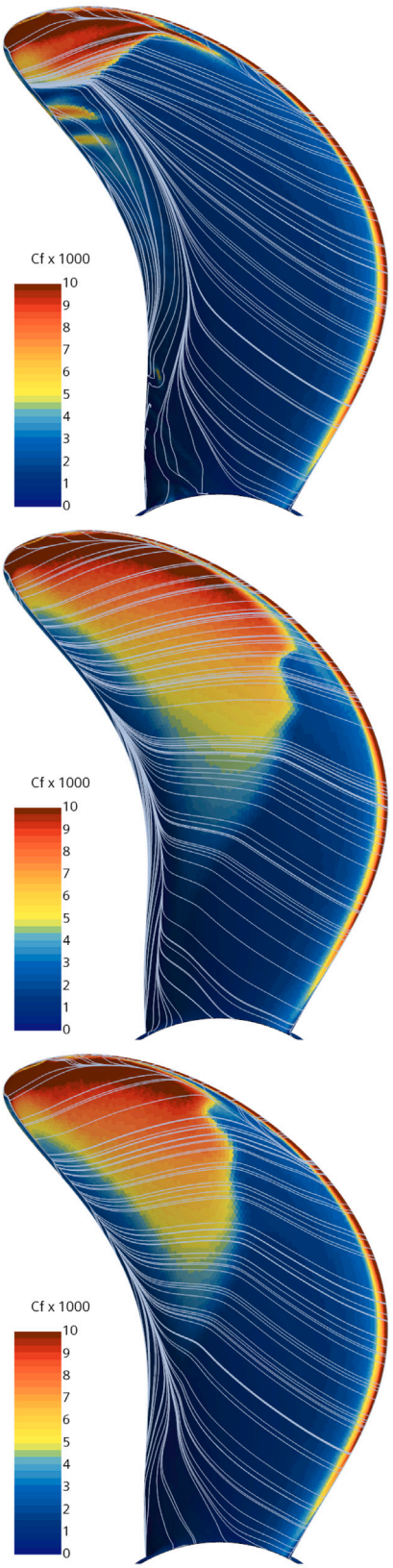

Fig. 8. Limiting streamlines and skin-friction coefficient on the suction side of the propeller blade at $J = 0.425$ without crossflow (top), with $CF1$ (middle) and with $CF2$ (bottom).

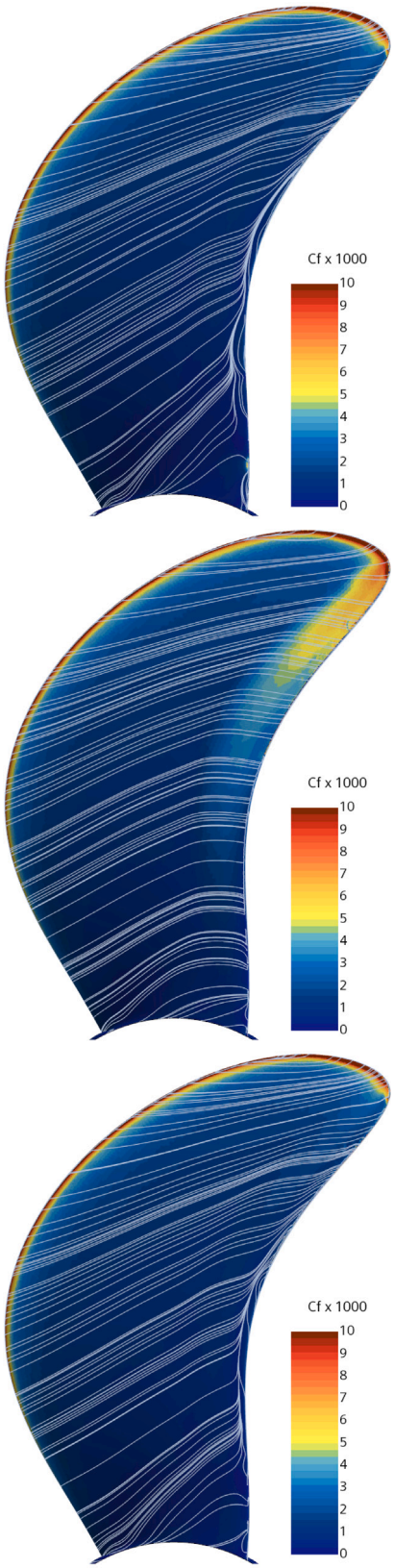

Fig. 9. Limiting streamlines and skin-friction coefficient on the pressure side of the propeller blade at $J = 0.425$ without crossflow (top), with $CF1$ (middle) and with $CF2$ (bottom).

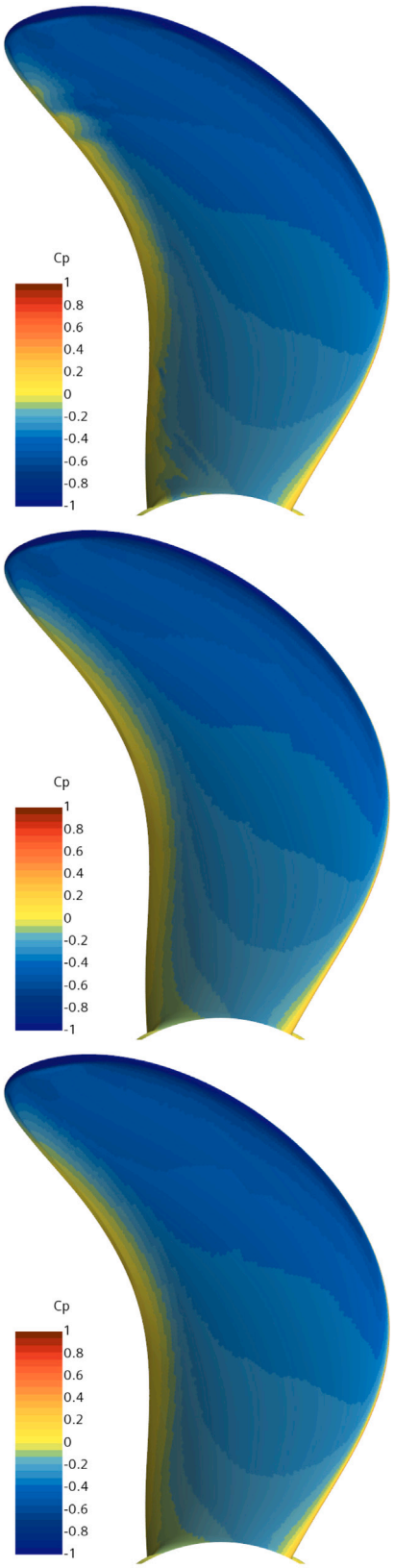

Fig. 10. Pressure coefficient on the suction side of the propeller blade at $J = 0.425$ without crossflow (top), with $CF1$ (middle) and with $CF2$ (bottom).

in Fig. 11. The situation resembles that discussed for the pressure side of the blade at $J = 0.425$, with the simulation with $CF1$ exhibiting transition near the trailing edge, which avoids the large region of separated flow that extends from the tip to almost the root of the blade, visible in the simulations without crossflow and those with $CF2$. On the other hand, on the pressure side of the blade, illustrated in Fig. 12, the simulation without crossflow exhibits transition and turbulent flow near the tip of the blade, besides a small region of separated flow near the trailing edge. When crossflow is included, a larger extent of turbulent flow is observed, and for both crossflow terms, the separated flow region at the trailing edge is prevented. As before, $CF1$ results in a slightly larger extent of turbulent flow and earlier transition than $CF2$.

It is curious to note that the situation at $J = 0.835$ seems similar to that showed for $J = 0.425$, exchanging the pressure and suction sides of the blade. However, bringing up the performance of the propeller again, at $J = 0.835$, the largest difference in K_T and K_Q relative to the simulations without crossflow were observed for $CF2$ and not for $CF1$. This might seem contradictory when taking into account that the flow over the blade obtained with $CF2$ shows more similarities with the solution without crossflow than the solution with $CF1$ does. However, it is highlighted that in the simulation with $CF2$, the flow separates on the suction side and not on the pressure side, causing a strong decrease in thrust and torque. In the case of the simulation with $CF1$, the flow does not separate on either side, so the effect balances out, thus resulting in smaller differences. The overall behaviour of the propeller performance and the flow regime on the blade for the two crossflow terms shows not only its importance, but also how apparently small changes can lead to significantly different results.

With these observations in mind, it is worth illustrating the importance of correctly applying the crossflow extension, and to discuss how it is influenced by the inlet turbulence intensity. Starting with the first aspect, Fig. 13 exhibits the skin friction coefficient on the surface of the blade, for $J = 0.425$ and the default implementation of the $CF1$ term, which computes the wrong helicity. The consequence, and similarly to what occurred in the prolate spheroid case, is an over-prediction of the extent of turbulent flow and too early transition on both sides of the blade. The suction side exhibits almost fully turbulent flow, a solution that almost resembles a simulation performed without a transition model. The effect on the pressure side is not as pronounced, but it is still a significant over-prediction when compared to the correct simulation whose results have been previously shown in Figs. 8 and 9. The same exercise was performed at $J = 0.835$, and the conclusions were similar, with almost fully turbulent flow on the pressure side, and a large extent of turbulent flow on the suction side. Logically, this effect also extends to the performance of the propeller, with a reduction on the predicted thrust coefficient of 1.7% for $J = 0.425$ and 3% for $J = 0.835$. Regarding K_Q, the effect is smaller with a 0.9% decrease on the lowest advance coefficient and 0.4% on the highest J.

So far, the influence of the inlet turbulence quantities has not been discussed, even though it can play a crucial role in the use of transition models. In order to make a brief assessment of their impact for this case, simulations were performed using $I = 3\%$ and a eddy viscosity ratio of 500 for all three modelling approaches. The limiting streamlines and C_f on the surface of the blade is shown in Fig. 14 for the suction side and in Fig. 15 for the pressure side. Despite the significant increase of the turbulence quantities, the changes in the flow field are small, when compared to the results presented previously in Figs. 11 and 12. The main difference lies in the occurrence of transition near the root of the blade when any crossflow term is active. On the other hand, almost no change at all is observed when crossflow is not included in the formulation.

A comparison of K_T and K_Q shows differences smaller than 2.5% for the simulations without crossflow, and lower than 0.1% when considering only the pressure components, when compared to the initial calculations using lower values of the turbulence quantities. The differences observed with $CF1$ range up to 9% for the friction

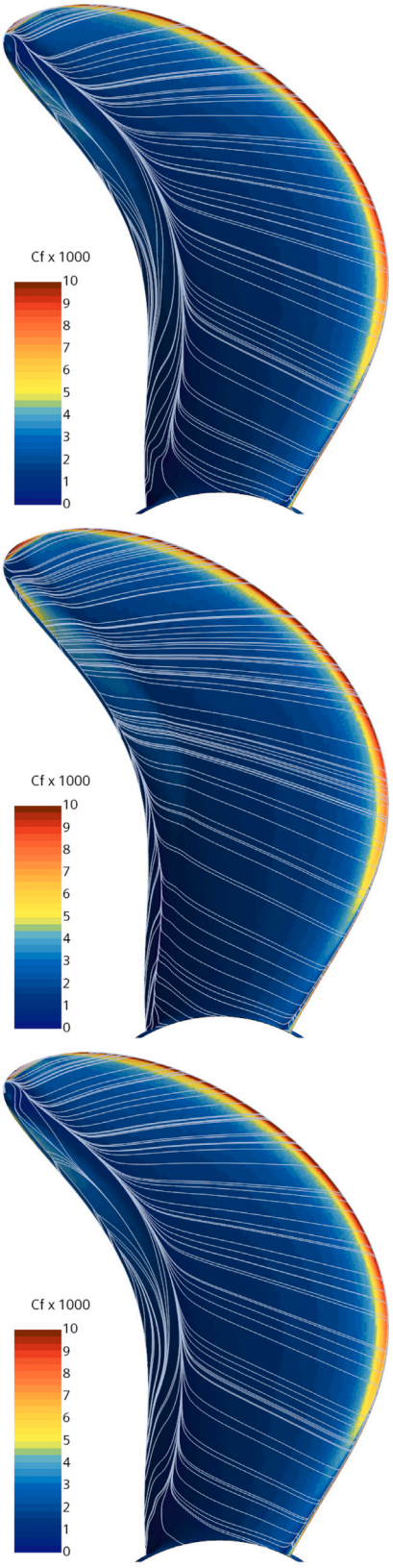

Fig. 11. Limiting streamlines and skin-friction coefficient on the suction side of the propeller blade at $J = 0.835$ without crossflow (top), with $CF1$ (middle) and with $CF2$ (bottom).

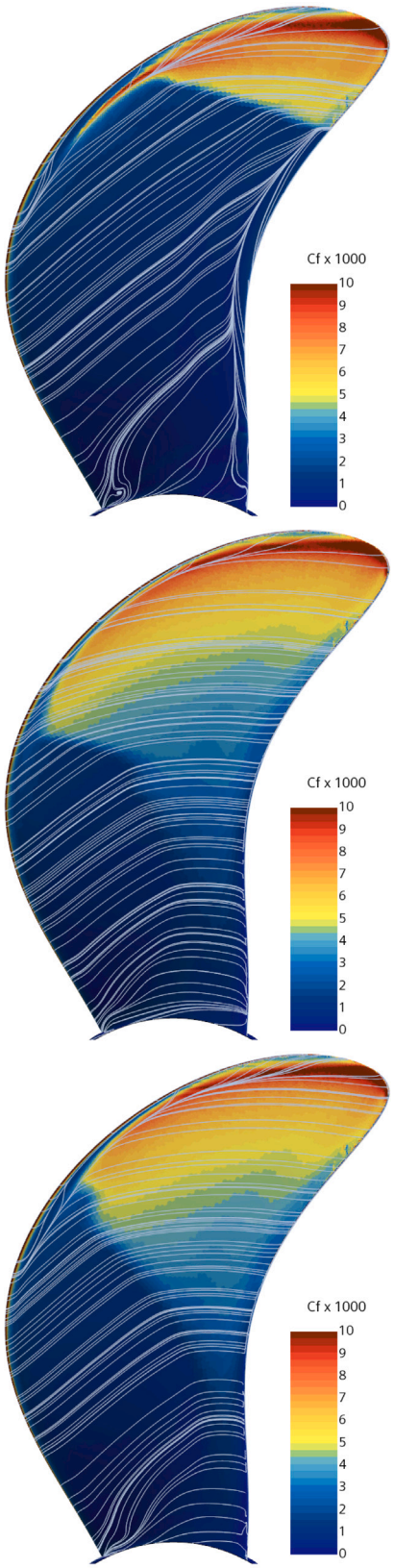

Fig. 12. Limiting streamlines and skin-friction coefficient on the pressure side of the propeller blade at $J = 0.835$ without crossflow (top), with $CF1$ (middle) and with $CF2$ (bottom).

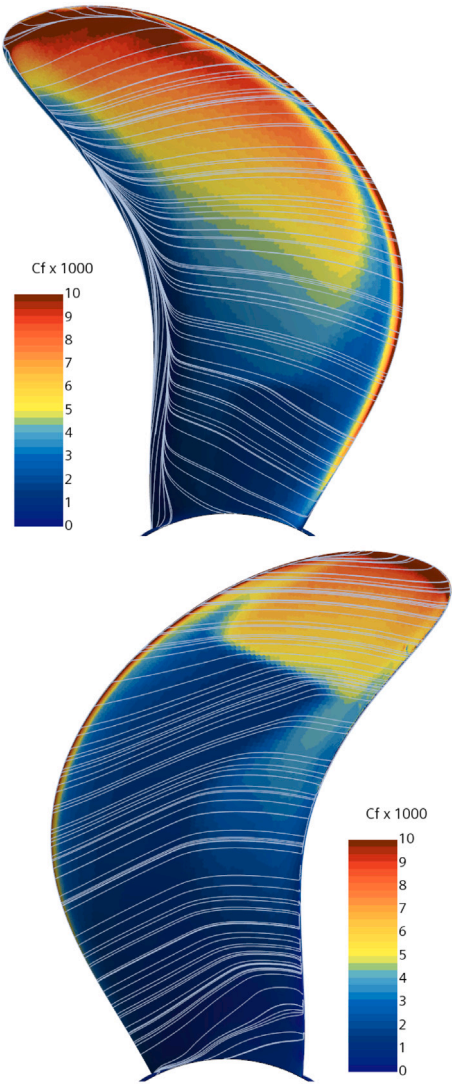

Fig. 13. Limiting streamlines and skin-friction coefficient on the suction (top) and pressure (bottom) sides of the propeller blade at $J = 0.425$ with the incorrect calculation of the helicity using $CF1$.

contribution and 1.4% for the pressure component. The $CF2$ model is the most affected, with a change in the friction component of up to 18% for the friction thrust and 5% for the pressure contribution of the thrust. This shows the $CF2$ extension to be the most affected by the change in the turbulence quantities than the remaining simulations, at least for the variation considered. It is noted that performing a similar study at $J = 0.425$ shows a smaller influence of the freestream turbulence, with minimal changes in the solutions obtained without crossflow and with $CF1$. The largest changes were observed in the friction contributions of thrust and torque for $CF2$.

The final part of the discussion focuses on the roughness height required by the $CF1$ model. All the previous simulations were performed with the default value of $h = 3 \times 10^{-6}$ m, which results in $C_r = 2$. A variation of h was conducted so that C_r varied from 1 to 2, the possible range according to Eq. (12). For this study, the base values of $I = 1\%$ and viscosity ratio of 1.0 were used for the turbulence quantities at the inlet. Fig. 16 illustrates the limiting streamlines and C_f on the pressure side of the blade for varying levels of h, or equivalently, C_r. As expected, the decrease of C_r tends to delay transition and leads to an overall decrease of C_f. For the lowest value of h, which corresponds to $C_r = 1$, laminar to turbulent transition is limited to the region near the

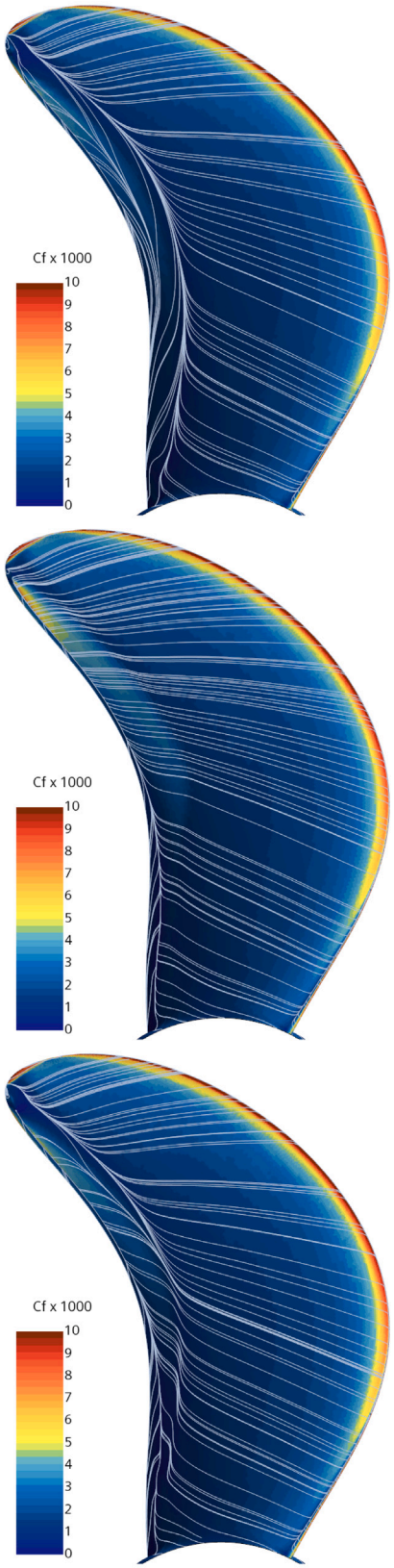

Fig. 14. Limiting streamlines and skin-friction coefficient on the suction side of the propeller blade at $J = 0.835$ without crossflow (top), with $CF1$ (middle) and with $CF2$ (bottom) for the inlet conditions with higher turbulence quantities.

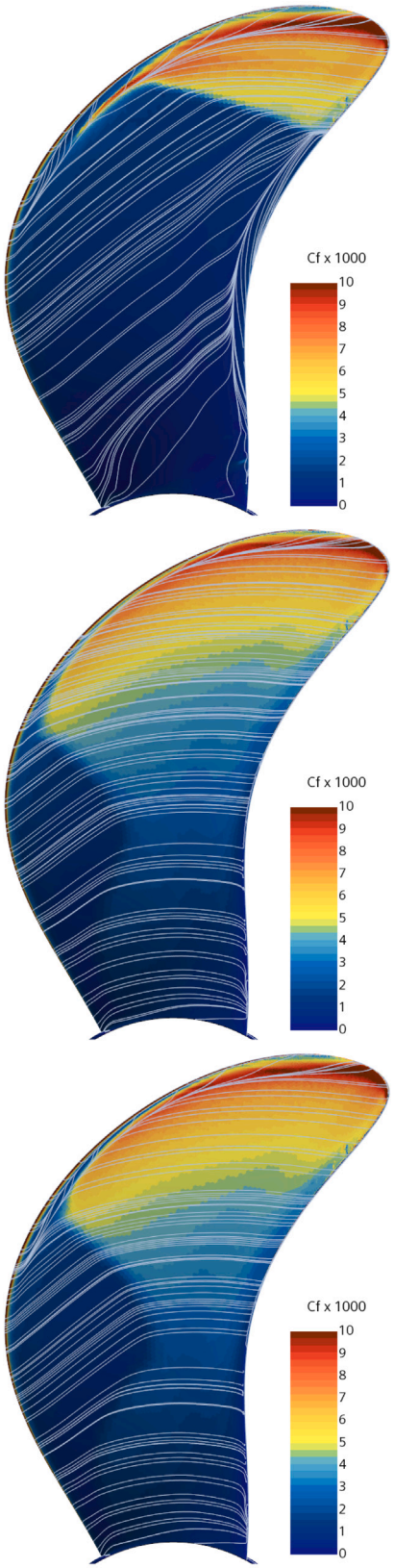

Fig. 15. Limiting streamlines and skin-friction coefficient on the pressure side of the propeller blade at $J = 0.835$ without crossflow (top), with $CF1$ (middle) and with $CF2$ (bottom) for the inlet conditions with higher turbulence quantities.

tip of the blade, and a small region of separated flow appears near the trailing edge of the blade. This behaviour is similar to that previously exhibited by $CF2$ in Fig. 9. Regarding the suction side of the propeller, there is only a small shift of transition downstream. Simulations were also performed for $J = 0.835$ with the same roughness variation, and the trend was similar to that discussed for Fig. 16. In the pressure side there is only a small change of transition upstream with the reduction of C_r. There is also a decrease in the extent of turbulent flow on the suction side. However, unlike what was obtained for $CF2$ and the solution without crossflow, which exhibited a large region of separated flow near the trailing edge, this is still avoided when using $CF1$, even for the lowest value of C_r.

Regarding the performance of the propeller when changing the roughness height, different trends were observed at $J = 0.425$ and at $J = 0.835$. On the lowest advance coefficient, decreasing h leads to an increase of the thrust and torque. This is in line with the initial expectation, since the decrease in h should lead to a solution that is less affected by crossflow and therefore more similar to the calculation performed without a crossflow term, which exhibited higher torque and thrust. On the other hand, at the highest advance coefficient, the decrease of h also leads to a decrease of K_T and K_Q. While conflicting with the behaviour discussed for $J = 0.425$, we note that the decrease in the roughness height causes the solution to resemble more that obtained with $CF2$, which showed the largest difference from the baseline simulation without a transition model. It should be mentioned that the maximum difference is in the range of 1%, which despite not being significant, still serves to illustrate the trend. As before the opposing behaviours observed at the different advance coefficients are justified by the competing effects on the pressure and suction side of the blade.

6. Conclusions

This work deals with the simulation of a controllable pitch propeller at model scale, with a focus on the influence of crossflow transition. Simulations are performed using the $k-\omega$ SST turbulence model and the γ transition model, with two different approaches for the effects of crossflow. The first approach corresponds to the default crossflow term available in the flow solver, while the second crossflow extension is one available in the open literature. Baseline simulations without crossflow were performed as well.

Preliminary simulations on the flow over a prolate spheroid show that the default implementation of the crossflow term available in STAR-CCM+ produces solutions that depend on the reference frame considered, an aspect that is caused by the lack of Galilean invariance in the formulation of the crossflow extensions used in this work. It is was also observed that the incorrect use of the crossflow term causes an overestimation of the turbulent flow regime, a trend that was seen also for the propeller simulations. An approach to remedy this is proposed and tested, and the results obtained on the prolate spheroid confirm its application and provide confidence for its application on the propeller simulations.

The results obtained for the propeller simulations show that the use of a crossflow term has a strong effect on the numerical robustness of the simulations. The use of a crossflow term appeared to improve the iterative convergence of the simulations, due to the reduction of the extent of flow separation on the propeller blades and the promotion of turbulent flow. On the other hand, the estimated numerical uncertainty for the thrust and torque coefficients increased when a crossflow term was used. This was caused by the fact that transition occurred in some cases near mid-chord, an area of the domain where the grid is not as refined as the leading or trailing edge of the blade.

Regarding the performance of the propeller, it was observed that the inclusion of crossflow transition leads to a decrease in the thrust and torque coefficients due to the larger extent of turbulent flow observed on the surface of the blades, compared to the case where crossflow is

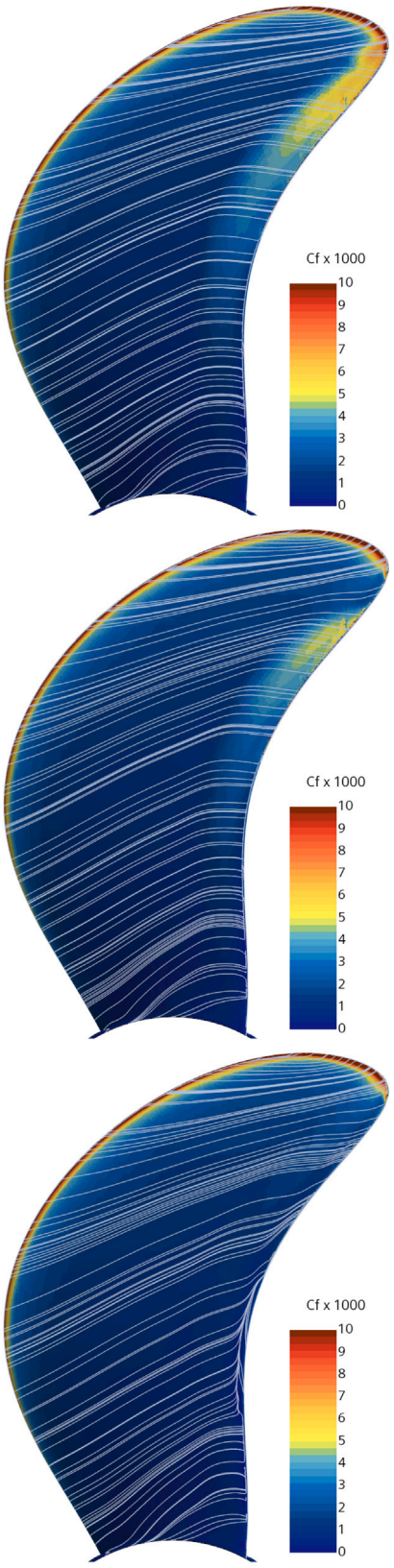

Fig. 16. Limiting streamlines and skin-friction coefficient on the pressure side of the propeller blade at $J = 0.425$ for $CF1$ with $C_r = 1.75$ (top), $C_r = 1.5$ (middle) and $C_r = 1$ (bottom).

not included. Another important factor affecting the performance of the propeller is the reduced extent of separated flow regions, due to transition taking place before laminar separation, usually near the trailing edge of the blade. The comparison between the two crossflow terms exhibited differences in the propeller performance that in some cases were larger than the differences towards the solution without crossflow. It was also observed that even though the crossflow extension $CF1$ always predicted earlier transition and a larger extent of turbulent flow than $CF2$, this not always led to larger differences compared to the simulations without crossflow. This is due to the effects of transition and flow separation on the suction and pressure sides of the blade, which are affected differently.

The study on the variation of the inlet turbulence quantities shows that for the present case, the large change in turbulent viscosity does not affect significantly the numerical predictions, both with and without crossflow. As a result, it is difficult to assess whether simulations with crossflow can be strongly affected by this parameter or not. Regardless, it is still mentioned that the largest effect was found on $CF2$. On the other hand, the $CF1$ crossflow term includes a user defined roughness parameter. The flow demonstrates some sensitivity to this parameter, with its decrease leading to reduced discrepancies between the two crossflow terms. Nonetheless, even at its minimum value, the $CF1$ crossflow term still predicted a larger extent of turbulent flow than $CF2$, and prevented laminar flow separation from occurring.

Overall, the presented results illustrate the importance of the inclusion of crossflow transition on simulations of model scale propellers when the flow is not tripped and avoid the fully laminar solution obtained with the baseline γ transition model. It is clear that even though the two crossflow formulations are built around the helicity as a driving parameter, they can lead to qualitatively different results. As a consequence, their specification is a crucial part of the mathematical formulation of the problem, which should not be neglected. On the same note, a correct implementation of the crossflow terms is required to avoid misleading results.

CRediT authorship contribution statement

Rui Lopes: Writing – original draft, Validation, Methodology, Investigation, Formal analysis, Conceptualization. **Arash Eslamdoost:** Writing – review & editing, Supervision, Resources, Methodology, Conceptualization. **Rikard Johansson:** Writing – review & editing, Supervision, Resources, Conceptualization. **Seemontini RoyChoudhury:** Writing – review & editing, Supervision, Resources, Conceptualization. **Rickard E. Bensow:** Writing – review & editing, Supervision, Project administration, Methodology, Funding acquisition, Conceptualization.

Declaration of competing interest

The authors declare that they have no known competing financial interests or personal relationships that could have appeared to influence the work reported in this paper.

Acknowledgements

This research is supported by the Swedish Energy Agency through project P2021-00277 and by Kongsberg Maritime Sweden AB through the University Technology Centre in Computational Hydrodynamics hosted by the Department of Mechanics and Maritime Sciences at Chalmers. The computations were enabled by resources provided by Chalmers e-Commons at Chalmers.

References

Abu-Ghannam, B.J., Shaw, R., 1980. Natural transition of boundary layers — the effects of turbulence, pressure gradient, and flow history. J. Mech. Eng. Sci. 22 (5), 213–228.

Arnal, D., Habiballah, M., Coustols, E., 1984. Théorie de l'instabilité laminaire et critères de transition en écoulement bi et tridimensionnel. La Recherche Aérosp. (2), 125–143.

Baltazar, J., Melo, D., Rijpkema, D., 2020. Analysis of the blade boundary-layer flow of a marine propeller using a RANS solver. Ocean Eng. 211, 107633.

Baltazar, J., Rijpkema, D., de Campos, J.F., 2018. On the use of the γ- $\tilde{Re}_{\theta_t}$ transition model for the prediction of the propeller performance at model-scale. Ocean Eng. 170, 6–19.

Baltazar, J., Rijpkema, D., Falcão de Campos, J., 2021. Prediction of the propeller performance at different Reynolds number regimes with RANS. J. Mar. Sci. Eng. 9 (10), 1115.

Bhattacharyya, A., Neitzel, J.C., Steen, S., Abdel-Maksoud, M., Krasilnikov, V., 2015. Influence of flow transition on open and ducted propeller characteristics. In: Fourth International Symposium on Marine Propulsors. Austin, Texas, USA.

Cakmakcioglu, S.C., Bas, O., Kaynak, U., 2018. A correlation-based algebraic transition model. Proc. Inst. Mech. Eng. C 232 (21), 3915–3929.

Coder, J.G., 2019. Further development of the amplification factor transport transition model for aerodynamic flows. In: AIAA Scitech 2019 Forum. p. 0039.

Coder, J.G., Maughmer, M.D., 2014. Computational fluid dynamics compatible transition modeling using an amplification factor transport equation. AIAA J. 52 (11), 2506–2512.

Coder, J.G., Maughmer, M.D., 2015. Application of the amplification factor transport transition model to the shear stress transport model. In: 53rd AIAA Aerospace Sciences Meeting. AIAA Paper 2015-0588, http://dx.doi.org/10.2514/6.2015-0588.

Crepier, P., 2017. Ship resistance prediction: verification and validation exercise on unstructured grids. In: MARINE VII: Proceedings of the VII International Conference on Computational Methods in Marine Engineering. CIMNE, pp. 365–376.

Denison, M., Pulliam, T.H., 2018. Implementation and assessment of the amplification factor transport laminar-turbulent transition model. In: 2018 Fluid Dynamics Conference. p. 3382. http://dx.doi.org/10.2514/6.2018-3382.

Eça, L., Hoekstra, M., 2014. A procedure for the estimation of the numerical uncertainty of CFD calculations based on grid refinement studies. J. Comput. Phys. 262, 104–130.

Gaggero, S., 2022. Influence of laminar-to-turbulent transition on model scale propeller performances. Part II: cavitating conditions. Ships Offshore Struct. 17 (4), 772–791.

Gaggero, S., Villa, D., 2018. Cavitating propeller performance in inclined shaft conditions with openfoam: PPTC 2015 test case. J. Mar. Sci. Appl. 17, 1–20.

Ge, M., Svennberg, U., Bensow, R.E., 2021. Improved prediction of sheet cavitation inception using bridged transition sensitive turbulence model and cavitation model. J. Mar. Sci. Eng. 9 (12), 1343.

Grabe, C., Shengyang, N., Krumbein, A., 2016. Transition transport modeling for the prediction of crossflow transition. In: 34th AIAA Applied Aerodynamics Conference. p. 3572. http://dx.doi.org/10.2514/6.2016-3572.

Jones, W.P., Launder, B.E., 1973. The calculation of low-Reynolds-number phenomena with a two-equation model of turbulence. Int. J. Heat Mass Transfer 16 (6), 1119–1130.

Langel, C.M., Chow, R., Van Dam, C.C.P., 2016. A comparison of transition prediction methodologies applied to high Reynolds number external flows. In: 54th AIAA Aerospace Sciences Meeting. p. 0551. http://dx.doi.org/10.2514/6.2016-0551.

Langtry, R., 2015. Extending the $\gamma - Re_\theta$ Correlation Based Transition Model for Crossflow Effects (Invited). In: 45th AIAA Fluid Dynamics Conference. http://dx.doi.org/10.2514/6.2015-2474.

Langtry, R.B., Menter, F.R., 2009. Correlation-based transition modeling for unstructured parallelized computational fluid dynamics codes. AIAA J. 47 (12), 2894–2906.

Li, D.-Q., Lindell, P., Werner, S., 2019. Transitional flow on model scale propellers and their likely influence on performance prediction. In: Proceedings of the Sixth International Symposium on Marine Propulsors. Rome, Italy.

Lopes, R., Eca, L., Kerkvliet, M., Toxopeus, S.L., 2022a. Predicting transition for the 6:1 prolate spheroid using the RANS equations. In: AIAA SCITECH 2022 Forum. p. 2570.

Lopes, R., Eça, L., Vaz, G., Kerkvliet, M., 2021. Assessing numerical aspects of transitional flow simulations using the RANS equations. Int. J. Comput. Fluid Dyn. 35 (3), 157–178.

Lopes, R., Eça, L., Vaz, G., Kerkvliet, M., 2022b. A technique to control the decay of freestream turbulence for transitional flow simulations. AIAA J. 60 (6), 3565–3580.

Medida, S., Baeder, J., 2011. Application of the correlation-based $\gamma - Re_\theta$ transition model to the spalart-allmaras turbulence model. In: 20th AIAA Computational Fluid Dynamics Conference. p. 3979. http://dx.doi.org/10.2514/6.2011-3979.

Menter, F.R., 1994. Two-equation eddy-viscosity turbulence models for engineering applications. AIAA J. 32 (8), 1598–1605.

Menter, F.R., Matyushenko, A., Lechner, R., Stabnikov, A., Garbaruk, A., 2022. An algebraic LCTM model for laminar–turbulent transition prediction. Flow Turbul. Combust. 109 (4), 841–869.

Menter, F.R., Smirnov, P.E., Liu, T., Avancha, R., 2015. A one-equation local correlation-based transition model. Flow Turbul. Combust. 95 (4), 583–619.

Minot, A., de Saint Victor, X., Marty, J., Perraud, J., 2015. Advanced numerical setup for separation-induced transition on high-lift low-pressure turbine flows using the γ-$\tilde{R}_{\theta_t}$ model. In: Turbo Expo: Power for Land, Sea, and Air, vol. 56642, American Society of Mechanical Engineers, http://dx.doi.org/10.1115/GT2015-42160, p. V02BT39A010.

Minot, A., Marty, J., Perraud, J., Casalis, G., 2017. Implementation of a surface roughness-based transition onset correction in the $\gamma - Re_\theta$ transition model. In: Turbo Expo: Power for Land, Sea, and Air. In: Turbomachinery, vol. 2B, http://dx.doi.org/10.1115/GT2017-63237.

Moran-Guerrero, A., Gonzalez-Gutierrez, L.M., Oliva-Remola, A., Diaz-Ojeda, H.R., 2018. On the influence of transition modeling and crossflow effects on open water propeller simulations. Ocean Eng. 156, 101–119.

Roache, P.J., 1998. Verification and Validation in Computational Science and Engineering. Hermosa Albuquerque, NM.

Rubino, G., Visonneau, M., 2022. Improved crossflow transition predictions for the one-equation γ transition model. Comput. & Fluids 245, 105580.

Rumsey, C.L., Pettersson Reif, B.A., Gatski, T.B., 2006. Arbitrary steady-state solutions with the k-ϵ model. AIAA J. 44 (7), 1586–1592.

Sheng, C., Wang, J., Zhao, Q., 2016. Improved rotor hover predictions using advanced turbulence modeling. J. Aircr. 53 (5), 1549–1560.

Smith, A.M.O., Gamberoni, N., 1956. Transition, Pressure Gradient and Stability Theory. Douglas Aircraft Co., Report ES 26388.

Sørensen, N.N., 2009. CFD modelling of laminar-turbulent transition for airfoils and rotors using the γ- model. Wind Energy Int. J. Prog. Appl. Wind Power Convers. Technol. 12 (8), 715–733.

Suzen, Y.B., Huang, P.G., 2000. Modeling of flow transition using an intermittency transport equation. J. Fluids Eng. 122 (2), 273–284.

van Ingen, J.L., 1956. A Suggested Semi-Empirical Method for the Calculation of the Boundary Layer Transition Region. Report VTH-74, Delft University of Technology.

Venkatachari, B.S., Paredes, P., Derlaga, J.M., Buning, P.G., Choudhari, M.M., Li, F., Chang, C.-L., 2021. Assessment of RANS-based transition models based on experimental data of the common research model with natural laminar flow. In: AIAA Scitech 2021 Forum. p. 1430. http://dx.doi.org/10.2514/6.2021-1430.

Viitanen, V., Siikonen, T., Sánchez-Caja, A., 2019. Numerical viscous flow simulations of cavitating propeller flows at different Reynolds numbers. In: Proceedings of the Sixth International Symposium on Marine Propulsors. Rome, Italy, pp. 26–30.

Walters, D.K., Cokljat, D., 2008. A three-equation eddy-viscosity model for Reynolds-averaged Navier-Stokes simulations of transitional flow. J. Fluids Eng. 130 (12), 121401.

Wang, X., Walters, K., 2012. Computational analysis of marine-propeller performance using transition-sensitive turbulence modeling. J. Fluids Eng. 134 (7), 071107.

Webster, J., Neu, W., Brizzolara, S., 2019. Reynolds stress transition modeling for marine propellers at low Reynolds number. In: Sixth International Symposium on Marine Propulsors. Smp19.

Wilcox, D.C., 2004. Turbulence Modeling for CFD, second ed. DCW Industries, Inc.

Zastawny, M., Lardeau, S., 2022. Validation of intermittency-based transition prediction models. In: AIAA SCITECH 2022 Forum. p. 2568. http://dx.doi.org/10.2514/6.2022-2568.